RSC Advances

PAPER

View Article Online
View Journal | View Issue

Cite this: *RSC Adv.*, 2021, **11**, 11779

Nanostructured RuO_2–Co_3O_4@RuCo-EO with low Ru loading as a high-efficiency electrochemical oxygen evolution catalyst†

Lingjun Tan, Ailian Zhang, Ziyi Liu, Ping'an Wei, Panpan Yang, Huan Guo, Hua Fang, Juanjuan Han, Yuchan Zhu * and Zhandong Ren

Received 12th January 2021
Accepted 17th March 2021

DOI: 10.1039/d1ra00271f

rsc.li/rsc-advances

Electrochemical water splitting technology is considered to be the most reliable method for converting renewable energy such as wind and solar energy into hydrogen. Here, a nanostructured RuO_2/Co_3O_4–RuCo-EO electrode is designed *via* magnetron sputtering combined with electrochemical oxidation for the oxygen evolution reaction (OER) in an alkaline medium. The optimized RuO_2/Co_3O_4–RuCo-EO electrode with a Ru loading of 0.064 mg cm^{-2} exhibits excellent electrocatalytic performance with a low overpotential of 220 mV at the current density of 10 mA cm^{-2} and a low Tafel slope of 59.9 mV dec^{-1} for the OER. Compared with RuO_2 prepared by thermal decomposition, its overpotential is reduced by 82 mV. Meanwhile, compared with RuO_2 prepared by magnetron sputtering, the overpotential is also reduced by 74 mV. Furthermore, compared with the RuO_2/Ru with core–shell structure (η = 244 mV), the overpotential is still decreased by 24 mV. Therefore, the RuO_2/Co_3O_4–RuCo-EO electrode has excellent OER activity. There are two reasons for the improvement of the OER activity. On the one hand, the core–shell structure is conducive to electron transport, and on the other hand, the addition of Co adjusts the electronic structure of Ru.

Introduction

Hydrogen is an ideal green energy carrier to replace fossil fuels. It has the characteristics of high energy density, storage, and no carbon emissions. Electrochemical water splitting technology is considered to be the most reliable method for converting renewable energy such as wind and solar energy into hydrogen. It is a very promising, sustainable, clean and efficient energy application strategy.[1–10] The electrolysis of water contains two half reactions, the oxygen evolution reaction (OER) at the anode and the hydrogen evolution reaction (HER) at the cathode. The main challenge of this technique is to reduce the excessive overpotential of HER and OER. The high overpotential of the OER reaction is the most important factor affecting the efficiency of water electrolysis.[11–20] Up to now, despite a lot of research, RuO_2 is still considered to be the most active electrocatalyst for OER. However, its overpotential is still not low enough, and it has disadvantages such as poor stability and high price, which still needs to be further improved.[21–25]

The introduction of abundant transition metal elements can improve the composition and structural of electrocatalysts, thereby improving OER activity and reducing costs.[26–30] Early literature reports have proved that the doping/alloying of transition metals such as Fe, Co, Ni, and Cu can optimize the local electronic and geometric structure of the original metal through the strain/ligand effect.[31–34] These changes will facilitate the chemical adsorption of intermediate adsorbed species (OH* and OOH*) on the surface of the electrocatalyst, which can increase the catalytic activity in an alkaline solution.[35] At the same time, all intermediate products interact with the metal oxide surface through oxygen atoms, and the bonding interaction (M–O) in the intermediate products (M–OH, M–O, and M–OOH) is very important for the overall OER activity. At present, more researches are focused on introducing metals into metal oxides, which can generate oxygen vacancies, thus regulating the adsorption of oxygen-containing intermediates at active sites. At the same time, the integrated electrocatalyst of metal and semiconductor can benefit the charge transfer process, that is, Mott–Schottky effect.

Previous literatures have shown that by changing the electronic structure of Ru, RuCo alloy can exhibit better OER activity.[36,38,40] At the same time, related literature has also proven that the rich metal–insulator interface structure is beneficial to improve the OER activity of Ru.[37,39] Therefore, it is hoped that both the Mott–Schottky effect will improve the charge transfer rate and the alloying will also optimize the electronic structure of Ru. This paper pays more attention to the preparation of the RuCo alloy base and the construction of the special surface morphology in the research method. At present,

School of Chemical and Environmental Engineering, Wuhan Polytechnic University, Wuhan, 430023, P. R. China. E-mail: zhuyuchan@163.com

† Electronic supplementary information (ESI) available. See DOI: 10.1039/d1ra00271f

for the preparation of this kind of catalyst, hydrothermal method combined with high-temperature calcination method is commonly used. But it has the disadvantages of long preparation time, high loading capacity, and the morphology of the obtained catalysts is mostly nanoparticles. Based on the above analysis, a new preparation method, that is, magnetron sputtering combined with electrochemical oxidation is investigated in this article. The method has the characteristics of short preparation time and low loading capacity. The prepared RuO_2/Co_3O_4–RuCo-EO electrode has a nanosheet and nanorod structure with Ru loading of 0.064 mg cm^{-2}, resulting in excellent OER activity with a low overpotential of only 220 mV at the current density of 10 mA cm^{-2} and Tafel slope of 59.9 mV dec^{-1} for OER.

Experimental

Electrode preparation

The Ti plate processed above was placed on the sample stage of the vacuum chamber. During the experiment, a Ru target with a purity of 99.99% and a Co target with a purity of 99.99% were used as sputtering targets. Evacuate the vacuum chamber to 4×10^{-4} Pa before sputtering. Then high-purity Ar gas was introduced, and the flow rate of argon gas was 30 mL min^{-1}. Adjust the pressure of the vacuum chamber to 1.0–1.2 Pa, and then the Ru target and the Co target were connected to the DC power supply for co-sputtering at the same time. The sputtering power of the Ru target was 60 W and the sputtering power of the Co target was 80 W. The co-sputtering was performed for 10 min. After the sputtering was completed, the resulting sample was recorded as the RuCo alloy catalyst. Next, it was calcined in a muffle furnace at 400 °C for 2 h, and the resulting sample was recorded as the RuO_2/Co_3O_4–RuCo catalyst.

The above RuO_2/Co_3O_4–RuCo catalyst was subjected to electrochemical oxidation (EO) process in a three-electrode system with the electrolyte 1.0 mol L^{-1} KOH solution. Before the EO process, adjust the temperature of the solution to 25 °C, and then pour argon gas with a purity of 99.999% into the solution for 15 minutes to remove dissolved oxygen from the solution. Then, using the RuO_2/Co_3O_4–RuCo catalyst as the working electrode, a multi-segment cyclic voltammetry (CV) scan was performed. The scanning range is 0–1.4 V (*vs.* RHE) and the scan rate is 100 mV s^{-1}. After the EO process, the obtained sample is recorded as RuO_2/Co_3O_4–RuCo-EO electrode. Among them, the samples with the number of CV scan of 200, 400, 600, 800 and 1000 segments are denoted as RuO_2/Co_3O_4–RuCo-EO-x (x = 200, 400, 600, 800 and 1000) electrodes. The preparation process of RuO_2/Ru and RuO_2 electrodes is described in ESI.†

Material characterization

X-ray diffraction (XRD) patterns were acquired on an XRD-7000 X-ray diffractometer. Scanning Electron Microscope (SEM) images were taken with a Zeiss ΣIGMA field-emission SEM. X-ray photoelectron spectrometry (XPS: ESCALAB 250Xi, Thermo Scientific) with monochromatized Al Kα radiation was used to analyze the electronic properties. Analysis of the composition of the electrode was carried out by X-ray fluorescence (XRF: EDX-7000, Shimadzu, Japan).

Electrochemical measurements

In the electrochemical experiment, a three-electrode system was used for testing on the CHI660 instrument. Among them, the working electrode are RuO_2/Co_3O_4–RuCo-EO, RuO_2/Co_3O_4–RuCo RuO_2/Ru and RuO_2 electrodes. In this paper, the Ru loading is about 0.064 mg cm^{-2} for different types of catalysts. The counter electrode is a carbon paper electrode. In order to avoid electrolyte contamination, the reference electrode is HgO/Hg/KOH (1.0 mol L^{-1}). The electrochemical characteristics of electrode materials were analyzed using cyclic voltammetry (CV) technology in 1.0 mol L^{-1} KOH solution. The OER activity was characterized by linear voltammetry scanning (LSV) in 1.0 mol L^{-1} KOH solution at a scanning speed of 5 mV s^{-1} in range of 1.2–1.8 V.

Results and discussion

Fig. 1 shows the different surface morphologies of RuO_2/Co_3O_4–RuCo before and after EO treatment. Fig. 1a and b are the scanning electron microscope (SEM) images of RuO_2/Co_3O_4–RuCo without EO treatment. It can be seen that the surface of the electrode is very smooth and the Ru and Co elements of RuO_2/Co_3O_4–RuCo electrode are evenly distributed (Fig. S1†). This is because the nanoclusters prepared by magnetron sputtering are very small, neatly arranged, and have good film-forming properties. However, after EO treatment, part of the cobalt on the electrode surface was oxidized and stripped at a high potential, resulting in a great change in the surface morphology. As shown in Fig. 1c and d, after CV scanning of 200 segments, a large number of two-dimensional nanosheets with a width of 200 nm and a thickness of 10 nm are formed on the surface of the RuO_2/Co_3O_4–RuCo-EO-200 electrode. After CV

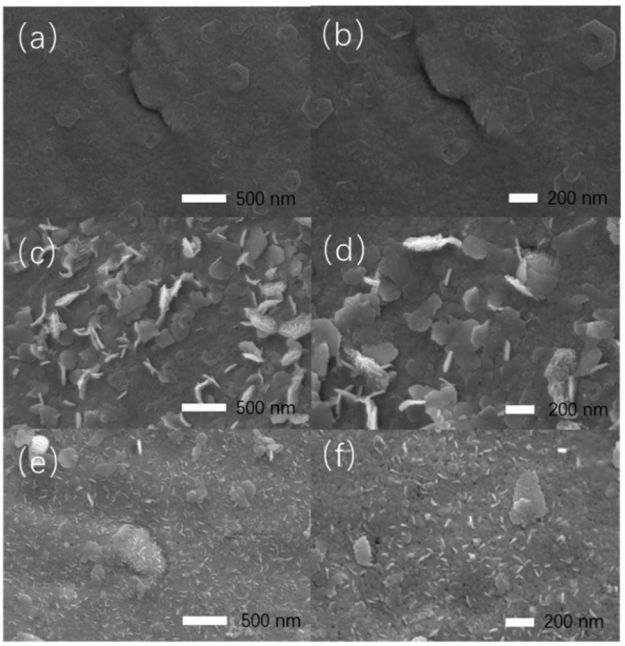

Fig. 1 SEM images of RuO_2/Co_3O_4–RuCo (a and b), RuO_2/Co_3O_4–RuCo-EO-200 (c and d) and RuO_2/Co_3O_4–RuCo-EO-1000 electrodes (e and f).

scanning of 1000 segments, most of the two-dimensional nanosheets were broken up, leaving a large number of small one-dimensional nanorods with a length of 100 nm on the surface of the RuO_2/Co_3O_4–RuCo-EO-1000 electrode (Fig. 1e and f). This can prove that the degree of oxidative exfoliation becomes more obvious as the number of CV cycles increases. In addition, the composition of Ru and Co of the electrodes before and after EO treatment is listed in Table S1.† Before EO treatment, the molar ratio of Ru and Co is 56 : 44. After CV scanning of 200, 400, 600, 800, and 1000 segments, the molar ratios of Ru and Co are 61 : 39, 66 : 34, 67 : 33, 67 : 33 and 65 : 35 respectively. This indicates that the EO treatment can reduce the Co content to a certain extent, but the composition ratio of Ru–Co under different CV cycles does not change much, but the morphology changes greatly.

Fig. 2 are the X-ray diffraction patterns (XRD) of RuO_2/Co_3O_4–RuCo-EO, accompanied by the comparison of those of RuO_2/Co_3O_4–RuCo and RuO_2/Ru. For RuO_2/Ru electrode, the diffraction peak at 44.0° is corresponding to the Ru(101) crystal plane (Fig. 2d), and the diffraction peak at 28.1° corresponds to the RuO_2(110) crystal plane (Fig. 2b). For RuO_2/Co_3O_4–RuCo electrode, the RuO_2(110) crystal plane is still observed at 28.1°. Meanwhile, due to the addition of Co, the (111) and (311) planes of Co_3O_4 are observed at 18.9° and 36.7° (Fig. 2a and c), respectively. However, these diffraction peaks above cannot be observed for RuCo electrode without thermal oxidation (Fig. S2†). Therefore, it can be confirmed that the RuCo alloy is first formed on the substrate by magnetron sputtering, and then the RuO_2/Co_3O_4–RuCo with a core–shell structure is obtained on the electrode surface with thermal oxidation of 400 °C. In addition, Ru and Co have formed bulk alloy and the characteristic crystal plane of RuCo alloy is located at 45.3° (Fig. S2†). After thermal oxidation and electrochemical oxidation, the peak of RuCo alloy is negatively shifted to 44.6° (Fig. 2d), which is still significantly positively shifted by 0.6° relative to the Ru(101) crystal plane. After EO treatment, no diffraction peak of Co_3O_4(111) crystal plane was found in the XRD pattern of RuO_2/Co_3O_4–RuCo-EO electrode, and the diffraction peak intensity of Co_3O_4(311) crystal plane was also not obvious. This is because Co_3O_4 on the surface of RuO_2/Co_3O_4–RuCo-EO electrode was oxidized and peeled off after EO treatment. At the same time, in order to verify the effect of EO treatment on the dissolution of Co on the surface, the XRD spectra of RuO_2/Co_3O_4–RuCo-EO after 200, 400, 600, 800 and 1000 segments of CV scans were also analyzed in Fig. 3. It is found that with the increase of the number of CV scan, the diffraction peak of Co_3O_4(111) crystal plane gradually weakens and disappears (Fig. 3a), which indicates that the number of CV scan is related to the degree of Co dissolution. Although the EO treatment has a significant effect on the structure of Co, it has no significant effect on the stable RuO_2 and RuCo alloy structure. The diffraction peaks of RuO_2(110) and RuCo alloy in the RuO_2/Co_3O_4–RuCo-EO electrode are still at 28.1° and 44.6° (Fig. 3b and d).

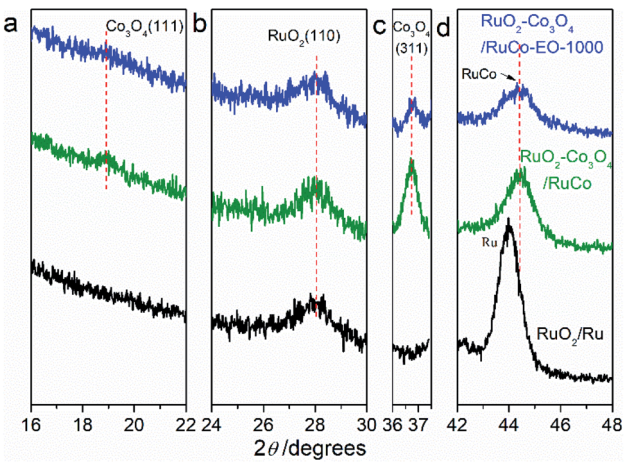

Fig. 2 X-ray diffraction patterns of RuO_2/Co_3O_4–RuCo-EO, RuO_2/Co_3O_4–RuCo and RuO_2/Ru electrodes. (a) Co_3O_4(111), (b) RuO_2(110), (c) Co_3O_4(311), (d) RuCo or Ru(101).

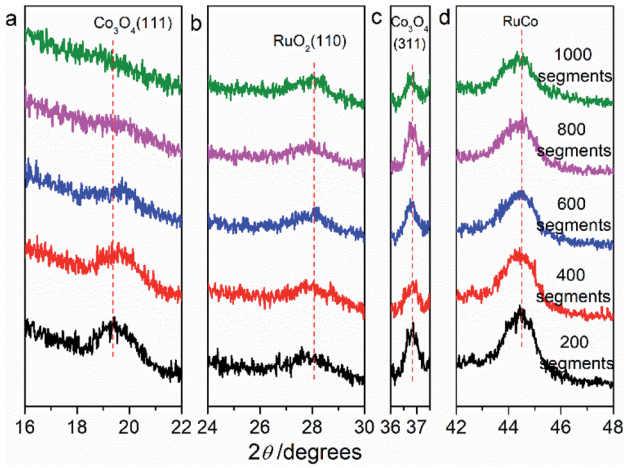

Fig. 3 X-ray diffraction patterns of RuO_2/Co_3O_4–RuCo-EO electrodes after CV scan of 200, 400, 600, 800 and 1000 segments. (a) Co_3O_4(111), (b) RuO_2(110), (c) Co_3O_4(311), (d) RuCo.

Fig. 4 are high-resolution X-ray photoelectron spectroscopy (XPS) spectra of RuO_2/Ru and RuO_2/Co_3O_4–RuCo-EO electrodes. As for RuO_2/Ru in Fig. 4a, the peaks at binding energies (BEs) of 484.5 and 462.2 eV are corresponding to the spin splitting peaks of $3p_{1/2}$ and $3p_{3/2}$ orbitals of Ru^0. Meanwhile, the peaks at 486.8 and 464.6 eV belong to the Ru^{4+} $3p_{1/2}$ and $3p_{3/2}$ orbitals, respectively. For RuO_2/Co_3O_4–RuCo-EO, the peaks position of Ru^{4+} spin orbitals are the same as those of RuO_2/Ru. However, the content of Ru^{4+} in RuO_2/Co_3O_4–RuCo-EO electrode is significantly higher than that of RuO_2/Ru electrode, indicating a higher degree of surface oxidation. In addition, the spin splitting peaks of Ru^0 $3p_{1/2}$ and $3p_{3/2}$ orbitals of RuO_2/Co_3O_4–RuCo-EO are located at 484.5 and 462.2 eV, respectively, which are positively shifted by 0.3 eV from those of RuO_2/Ru. In the high-resolution XPS spectrum of Co 2p of RuO_2/Co_3O_4–RuCo-EO (Fig. 4b), two peaks at binding energies (BEs) of 779.7 (781.1) and 794.6 (796.1) eV are corresponding to the spin orbitals of Co^{3+} (Co^{2+}) $2p_{3/2}$ and Co $2p_{1/2}$, accompanied by two weak satellite peaks at 789.1 and 804.7 eV. In Fig. 4c, the peak of 529.3 eV, 530.6 eV and 531.9 eV of RuO_2/Ru is attributed to O 1s orbital in O^{2-}, OH^- and H_2O, respectively. The peak of 529.8 eV,

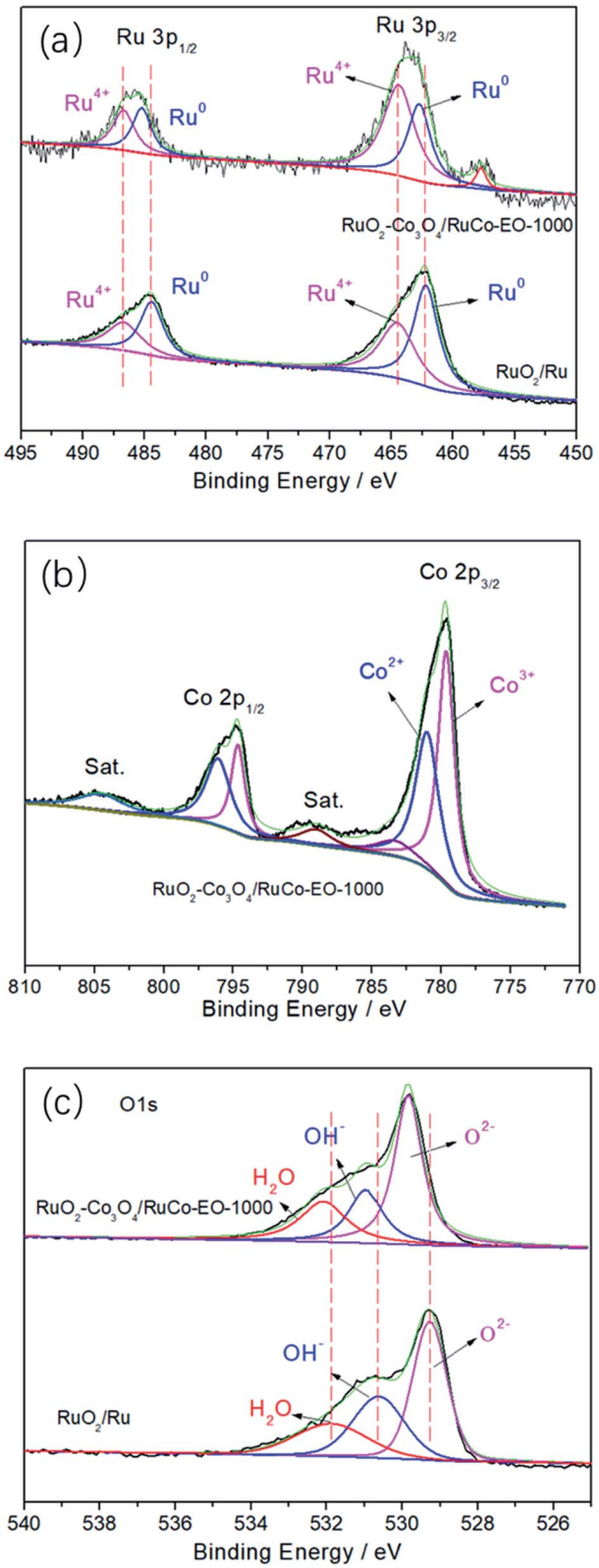

Fig. 4 High-resolution XPS spectra of Ru 3p (a), Co 2p (b) and O 1s (c) in the RuO_2/Co_3O_4–RuCo-EO electrode compared with those in RuO_2/Ru electrode.

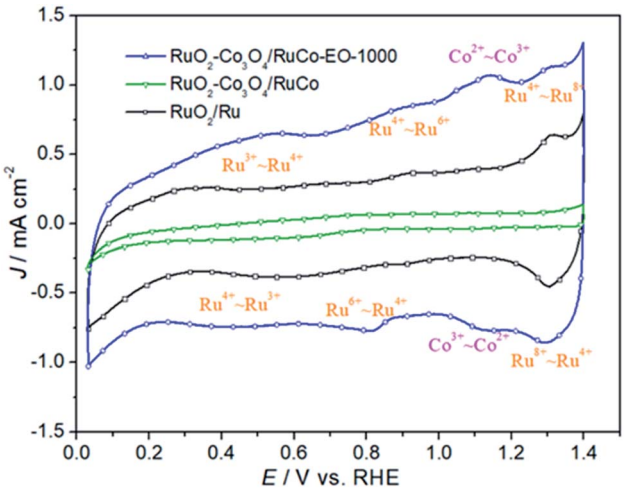

Fig. 5 The cyclic voltammetry curves of RuO_2/Co_3O_4–RuCo-EO, RuO_2/Co_3O_4–RuCo and RuO_2/Ru electrodes.

531.0 eV and 532.1 eV of RuO_2/Co_3O_4–RuCo-EO is attributed to O 1s orbital in O^{2-}, OH^- and H_2O, respectively.

Fig. 5 is the cyclic voltammetry (CV) curves of RuO_2/Ru, RuO_2/Co_3O_4–RuCo and RuO_2/Co_3O_4–RuCo-EO electrodes. First of all, it can be clearly seen that the double-layer current of the RuO_2/Co_3O_4–RuCo electrode is obviously lower than that of RuO_2/Ru, indicating that the electrochemical surface area (ECSA) of the RuO_2/Co_3O_4–RuCo electrode is small. The reason is that the surface of RuO_2/Co_3O_4–RuCo electrode obtained by high vacuum magnetron co-sputtering technology is extremely flat and smooth, as shown by SEM characterization in Fig. 1. However, after the EO treatment, the double-layer current of the RuO_2/Co_3O_4–RuCo-EO electrode has increased significantly, which is significantly larger than those of the other two electrodes. This indicates that the RuO_2/Co_3O_4–RuCo-EO electrode has a larger ECSA and can provide more electrochemically active sites. In addition, it can be seen from the Fig. 5 that the electrochemical characteristics of the RuO_2/Co_3O_4–RuCo-EO electrode are also obvious. Among them, the redox peaks at the potentials of 0.50 and 0.54 V are corresponding to the transition between Ru^{3+}–Ru^{4+}. And the redox process of Ru^{4+}–Ru^{6+} occur at 0.82 and 0.90 V. In the potential of 1.30 and 1.31 V, the redox reaction of Ru^{4+}–Ru^{8+} undergoes in this potential range. For the electrochemical characteristics of Co, the oxidation and reduction reactions of Co^{2+}–Co^{3+} occur at 1.12 and 1.14 V, respectively.

In order to investigate the oxygen evolution reaction (OER) activity of three catalysts, a linear sweep voltammetry tests were performed, as shown in Fig. 6. It can be seen from the figure that the OER activity of RuO_2/Co_3O_4–RuCo-EO electrode is significantly higher than that of RuO_2/Co_3O_4–RuCo electrode. For example, the current density of RuO_2/Co_3O_4–RuCo electrode at 1.8 V is 53.55 mA cm^{-2}, while the current density of RuO_2/Co_3O_4–RuCo-EO electrode is increased to 124.20 mA cm^{-2}, which is 2.32 times that of RuO_2/Co_3O_4–RuCo electrode. At the same time, when the current density reaches 10 mA cm^{-2}, the overpotential of RuO_2/Co_3O_4–RuCo and RuO_2/Co_3O_4–RuCo-EO

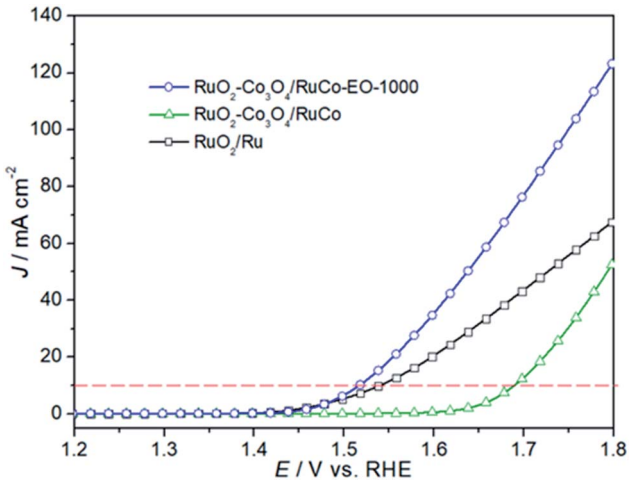

Fig. 6 The OER activities of RuO_2/Co_3O_4–RuCo-EO, RuO_2/Co_3O_4–RuCo and RuO_2/Ru electrodes.

electrodes are 394 and 220 mV, respectively. The latter is 174 mV lower than the former, indicating a significant increase in OER activity. This indicates that electrochemical oxidation can improve the OER activity of the catalyst. Furthermore, compared with the OER activity of RuO_2 prepared by thermal decomposition (Fig. S3†), the overpotential of RuO_2/Co_3O_4–RuCo-EO electrode is reduced by 82 mV. Compared with the OER activity of RuO_2 prepared by magnetron sputtering (Fig. S4†), the overpotential of RuO_2/Co_3O_4–RuCo-EO electrode is reduced by 74 mV. Compared with the OER activity of RuO_2/Ru (the overpotential of 244 mV), the overpotential of RuO_2/Co_3O_4–RuCo-EO electrode is still decreased by 24 mV. Therefore, it is proved once again that the OER activity of RuO_2/Co_3O_4–RuCo-EO electrode is indeed excellent.

There are two reasons for the improvement of the electrochemical activity of RuO_2/Co_3O_4–RuCo-EO electrode. On the one hand, the special core–shell structure of the electrode itself can facilitate the charge transfer process, and on the other hand, the addition of Co can change the electronic structure of Ru. For ordinary RuO_2, whether it is prepared by magnetron sputtering or thermal decomposition, there is only an oxide phase in its structure, but no metal phase (Fig. S5 and S6†). Therefore, their activity is generally lower than that of catalysts with a metal oxide/metal core–shell structure. Generally speaking, due to the good electronic interaction and charge transfer between metal and semiconductor at the metal–semiconductor interface, that is, the Mott–Schottky effect, the combination of metal and semiconductor in the electrocatalyst can facilitate the charge transfer process. On the other hand, RuO_2/Co_3O_4–RuCo-EO electrode has a high content of Ru oxidation state. It can be seen from the XPS spectrum (Fig. 4a) that the ratio of peak area of Ru^{4+}/Ru^0 in RuO_2/Co_3O_4–RuCo-EO electrode is significantly greater than the ratio of peak area in RuO_2/Co_3O_4–RuCo electrode. The spin splitting peaks of Ru^0 $3p_{1/2}$ and $3p_{3/2}$ of RuO_2/Co_3O_4–RuCo-EO are positively shifted by 0.3 eV compared to those of RuO_2/Ru, indicating that Ru transfers electrons to Co. Therefore, the d-band center of Ru will rise, and the adsorption of intermediate products will be enhanced, thereby increasing the OER activity. In addition, the increase in ECSA is also conducive to improving OER activity. As shown in Fig. S7,† the increase of ECSA is mainly reflected in the double-layer capacitance of RuO_2/Co_3O_4–RuCo-EO electrode, which is obviously larger than that of RuO_2/Co_3O_4–RuCo and RuO_2/Ru electrodes.

In order to further reveal the influence of the ECSA on the OER activity of the catalyst, the OER activities of RuO_2/Co_3O_4–RuCo-EO electrodes with different number of CV scan were studied. As shown in Fig. 7, when the CV scan is 200, 400, 600, 800, and 1000 segments, the OER current density of RuO_2/Co_3O_4–RuCo-EO electrode is 107.1, 114.5, 125.4, 128.8 and 124.2 mA cm^{-2}, respectively, at the potential of 1.8 V (*vs.* RHE). When the CV scan is between 200 and 800 segments, the current density of OER increases by about 10 mA cm^{-2} for every additional 200 segments. At the same time, the corresponding double-layer capacitance gradually increases, which means that the ECSA also gradually increases (Fig. S8†). This indicates that the OER activity increases continuously with the increase of the ECSA. When the CV scan is 1000 segments, the surface of RuO_2/Co_3O_4–RuCo-EO electrode tends to be stable, then the ECSA no longer increases, and the OER activity no longer increases. In

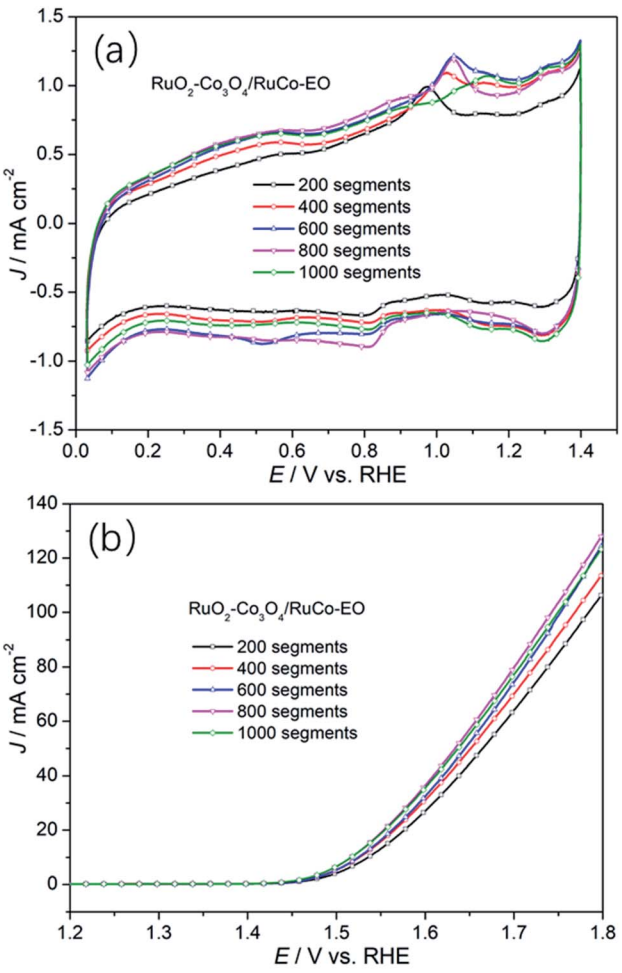

Fig. 7 The cyclic voltammetry curves (a) and OER activities (b) of RuO_2/Co_3O_4–RuCo-EO with different segment of CV scan.

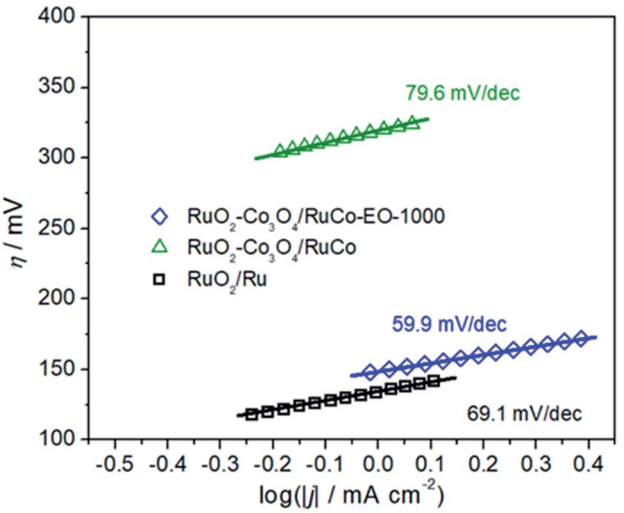

Fig. 8 The Tafel slopes of RuO_2/Co_3O_4–RuCo-EO, RuO_2/Co_3O_4–RuCo and RuO_2/Ru electrodes.

addition, it can also be observed in Fig. S9† the oxidation potential of Co gradually increases with the increase of CV scan, which means that the oxidation stripping is more thorough. In addition, the Co content also has an important influence on OER activity (Fig. S10†). When the Co content is low, it has little effect on the structure and morphology of the RuO_2/Co_3O_4–RuCo-EO electrode, and the OER activity is low. However, when the Co content is high, the OER activity of RuO_2/Co_3O_4–RuCo-EO electrode is also poor, because the OER activity of Co itself is poor. When the Co content is 35% after EO treatment of 1000 segments, the OER activity of the RuO_2/Co_3O_4–RuCo-EO electrode is the best.

Finally, the surface morphology of the catalyst also has a significant impact on the activity. Regarding the RuO_2 electrode, whether it is prepared by magnetron sputtering or thermal decomposition, the surface appears as a nanosphere with a diameter of 50–100 nm (Fig. S11 and S12†). The surface morphology of RuO_2/Ru electrode prepared by magnetron sputtering also presents a smooth surface, with a particle size of 20–50 nm (Fig. S13†). However, the RuO_2/Co_3O_4–RuCo-EO electrode prepared above has exhibited a porous nanosheet (Fig. 1c and d) or nanorod structure (Fig. 1e and f). The difference in morphology will bring about different OER activities.

In order to explore the reason for the increase in its intrinsic activity, Tafel analysis was finally performed to determine the reaction mechanism (Fig. 8). The Tafel slopes of RuO_2/Co_3O_4–RuCo and RuO_2/Ru are 79.6 and 69.1 mV dec^{-1}, respectively. However, the Tafel slope of RuO_2/Co_3O_4–RuCo-EO is only 59.9 mV dec^{-1}. The lower Tafel slope indicates that the RuO_2/Co_3O_4–RuCo-EO electrode has higher OER activity. The rate determination step of the OER process should be determined as the formation of OH_{ads}. The above discussion will be studied in detail in subsequent experiments. Finally, the stability of the RuO_2/Co_3O_4–RuCo-EO electrode was also investigated in Fig. S14.† After 13 h of chronopotentiometry measurement at current density of 10 mA cm^{-2}, the OER activity was basically stable.

Conclusions

In this article, a new RuO_2/Co_3O_4–RuCo-EO electrode is designed *via* a magnetron sputtering combined with electrochemical oxidation for OER in an alkaline medium. The optimized RuO_2/Co_3O_4–RuCo-EO electrode has exhibited excellent electrocatalytic performance with a low overpotential of 220 mV and Tafel slope of 59.9 mV dec^{-1} for OER at the current density of 10 mA cm^{-2}. Compared with RuO_2 prepared by thermal decomposition, its overpotential is reduced by 82 mV. Meanwhile, compared with RuO_2 prepared by magnetron sputtering, its overpotential is also reduced by 74 mV. Compared with RuO_2/Ru (the overpotential of 244 mV), the overpotential is still decreased by 24 mV. There are two reasons for the improvement of the electrochemical activity of RuO_2/Co_3O_4–RuCo-EO electrode. On the one hand, the metal oxide–metal with core–shell structure is conducive to electron transport, and on the other hand, the addition of Co changes the electronic structure of Ru. The positive shift of the spin splitting peaks of Ru indicates that Ru transfers electrons to Co. Therefore, the d-band center of Ru will rise, and the adsorption of intermediate products will be enhanced, thereby increasing the OER activity. In addition, the increase in ECSA is also conducive to improving OER activity.

Conflicts of interest

There are no conflicts to declare.

Acknowledgements

The authors would like to acknowledge financial support from the Natural Science Foundation of Hubei Province (2020CFB777).

Notes and references

1 J. Wang, W. Cui, Q. Liu, Z. Xing, A. M. Asiri and X. Sun, *Adv. Mater.*, 2016, **28**, 215–230.
2 X. Tian, P. Zhao and W. Sheng, *Adv. Mater.*, 2019, **31**, 1808066.
3 E. Liu, J. Li, L. Jiao, H. Doan, Z. Liu, Z. Zhao, Y. Huang and K. M. Abraham, *J. Am. Chem. Soc.*, 2019, **141**, 3232–3239.
4 Z. Yao, J. Yan, V. Anthony and S. Z. Qiao, *Angew. Chem., Int. Ed.*, 2018, **57**, 7568–7579.
5 J. Liu, Y. Liu, N. Liu, Y. Han, X. Zhang, H. Huang, Y. Lifshitz, S. Lee, J. Zhong and Z. Kang, *Science*, 2015, **347**, 970.
6 S. T. Hunt, M. Milina, Z. Wang and Y. R. Leshkov, *Energy Environ. Sci.*, 2016, **9**, 3290–3301.
7 N. Yao, P. Li, Z. Zhou, Y. Zhao, G. Cheng, S. Chen and W. Luo, *Adv. Energy Mater.*, 2019, **9**, 1902449.
8 X. Zou and Y. Zhang, *Chem. Soc. Rev.*, 2015, **44**, 5148–5180.
9 J. Wang, F. Xu, H. Jin, Y. Chen and Y. Wang, *Adv. Mater.*, 2017, **29**, 1605838.
10 M. Wang, L. Chen and L. Sun, *Energy Environ. Sci.*, 2012, **5**, 6763–6778.
11 S. Zhao, J. Huang, Y. Liu, J. Shen, H. Wang, X. Yang, Y. Zhu and C. Li, *J. Mater. Chem. A*, 2017, **5**, 4207–4214.

12 D. Li, Z. Zong, Z. Tang, Z. Liu, S. Chen, Y. Tian and X. Wang, *ACS Sustainable Chem. Eng.*, 2018, **6**, 5105–5114.
13 L. Li, B. Wang, G. Zhang, G. Yang, T. Yang, S. Yang and S. Yang, *Adv. Energy Mater.*, 2020, **10**, 2001600.
14 G. Li, S. Li, J. Ge, C. Liu and W. Xing, *J. Mater. Chem. A*, 2017, **5**, 17221–17229.
15 L. Gloag, T. M. Benedetti, S. Cheong, R. F. Webster, C. E. Marjo, J. J. Gooding and R. D. Tilley, *Nanoscale*, 2018, **10**, 15173–15177.
16 Z. Wang, S. M. Xu, Y. Xu, L. Tan, X. Wang, Y. Zhao, H. Duan and Y. F. Song, *Chem. Sci.*, 2019, **10**, 378–384.
17 F. M. Mota, C. H. Choi, R. Boppella, J. E. Lee and D. H. Kim, *J. Mater. Chem. A*, 2019, **7**, 639–646.
18 Z. Liu, M. Zha, Q. Wang, G. Hua and L. Feng, *Chem. Commun.*, 2020, **56**, 2352–2355.
19 Z. Li, S. Wang, Y. Tian, B. Li, H. Yan, S. Zhang, Z. Liu, Q. Zhang, Y. Lin and L. Chen, *Chem. Commun.*, 2020, **56**, 1749–1752.
20 L. Fagiolari, F. Zaccaria, F. Costantino, R. Vivani, C. Mavrokefalos, G. R. Patzked and A. Macchioni, *Dalton Trans.*, 2020, **49**, 2468–2476.
21 S. Laha, Y. Lee, F. Podjaski, D. Weber, V. Duppel, L. M. Schoop, F. Pielnhofer, C. Scheurer, K. Müller, U. Starke, K. Reuter and B. V. Lotsch, *Adv. Energy Mater.*, 2019, **9**, 1803795.
22 J. Yu, Q. He, G. Yang, W. Zhou, Z. Shao and M. Ni, *ACS Catal.*, 2019, **9**, 9973–10011.
23 J. Su, R. Ge, K. Jiang, Y. Dong, F. Hao, Z. Tian, G. Chen and L. Chen, *Adv. Mater.*, 2018, **30**, 1801351.
24 K. Yang, P. Xu, Z. Lin, Y. Yang, P. Jiang, C. Wang, S. Liu, S. Gong, L. Hu and Q. Chen, *Small*, 2018, **14**, 1803009.
25 M. Retuerto, L. Pascual, C. Federico, P. Ferrer, D. Gianolio, A. G. Pereira, Á. García, J. Torrero, T. F. María, P. Bencok, M. A. Peña, J. L. Fierro and S. Rojas, *Nat. Commun.*, 2019, **10**, 2041.
26 R. Farhat, J. Dhainy and L. Halaoui, *ACS Catal.*, 2020, **10**, 20–35.
27 Q. Yang, P. Jin, B. Liu, L. Zhao, J. Cai, Z. Wei, S. Zuo, J. Zhang and L. Feng, *J. Mater. Chem. A*, 2020, **8**, 9049–9057.
28 Y. Wang, P. Zheng, M. Li, Y. Li, X. Zhang, J. Chen, X. Fang, Y. Liu, X. Yuan, X. Dai and H. Wang, *Nanoscale*, 2020, **12**, 9669–9679.
29 T. Zhu, J. Huang, B. Huang, N. Zhang, S. Liu, Q. Yao, S. Haw, Y. Chang, C. W. Pao, J. M. Chen, Q. Shao, Z. Hu, Y. Ma and X. Huang, *Adv. Energy Mater.*, 2020, **10**, 2002860.
30 A. Yu, C. Lee, M. H. Kim and Y. Lee, *ACS Appl. Mater. Interfaces*, 2017, **9**, 35057–35066.
31 C. Gao, H. Wang, S. Li, B. Liu, J. Yang, J. Gao, Z. Peng, Z. Zhang and Z. Liu, *Electrochim. Acta*, 2019, **327**, 134958.
32 Q. Wu, M. Luo, J. Han, W. Peng, Y. Zhao, D. Chen, M. Peng, J. Liu, F. M. F. Groot and Y. Tan, *ACS Energy Lett.*, 2020, **5**, 192–199.
33 X. Sun, F. Liu, X. Chen, C. Li, J. Yu and M. Pan, *Electrochim. Acta*, 2019, **307**, 206–213.
34 H. Wang, Y. Yang, F. DiSalvo and H. D. Abruna, *ACS Catal.*, 2020, **10**, 4608–4616.
35 R. P. Gautam, H. Pan, F. Chalyavi, M. J. Tucker and C. J. Barile, *Catal. Sci. Technol.*, 2020, **10**, 4960–4967.
36 H. Liu, X. Li, L. Ge, C. Peng, L. Zhu, W. Zou, J. Chen, Q. Wu, Y. Zhang, H. Huang, J. Wang, Z. Cheng, Z. Fu and Y. Lu, *Catal. Sci. Technol.*, 2020, **10**, 8314–8324.
37 X. Gao, J. Chen, X. Sun, B. Wu, B. Li, Z. Ning, Z. Li and N. Wang, *ACS Appl. Nano Mater.*, 2020, **3**, 12269–12277.
38 Y. Bao, J. Dai, J. Zhao, Y. Wu, C. Li, L. Ji, X. Zhang and F. Yang, *ACS Appl. Energy Mater.*, 2020, **3**, 1869–1874.
39 Z. Fan, J. Jiang, L. Ai, Z. Shao and S. Liu, *ACS Appl. Mater. Interfaces*, 2019, **11**, 47894–47903.
40 T. Feng, G. Yu, S. Tao, S. Zhu, R. Ku, R. Zhang, Q. Zeng, M. Yang, Y. Chen, W. Chen, W. Chen and B. Yang, *J. Mater. Chem. A*, 2020, **8**, 9638–9645.